Thoracic EIT in 3D – experiences and recommendations

Bartłomiej Grychtol[1,2], Johannes Peter Schramel[3], Fabian Braun[4], Thomas Riedel[5,6], Ulrike Auer[3], Martina Mosing[7], Christina Braun[3], Andreas D. Waldmann[8], Stephan H. Böhm[8], Andy Adler[9]

[1] Fraunhofer Project Group for Automation in Medicine and Biotechnology, Mannheim, Germany
[2] Medical Faculty Mannheim, University of Heidelberg, Mannheim, Germany
[3] Vetmeduni Vienna, Anaesthesiology and Perioperative Intensive Care Medicine
[4] Centre Suisse d'Electronique et de Microtechnique, Neuchâtel, Switzerland
[5] Paediatric Pulmonology, University Children's Hospital and University of Bern, Switzerland
[6] Department of Paediatrics, Cantonal Hospital Graubuenden, Chur, Switzerland
[7] School of Veterinary and Life Sciences, Murdoch University, Perth, Australia
[8] Department of Anesthesiology and Intensive Care Medicine, Rostock University Medical Center, Germany
[9] Systems and Computer Engineering, Carleton University, Ottawa, Canada

E-mail: `Andy.Adler@Carleton.ca`

Abstract.

Objective In EIT applications to the thorax, a single electrode plane has typically been used to reconstruct a transverse 2D "slice". However, such images can be misleading as EIT is sensitive to contrasts above and below the electrode plane, and ventilation and aeration inhomogeneities can be distributed in complex ways. Using two (or more) electrode planes, 3D EIT images may be reconstructed, but 3D reconstructions are currently little used in thoracic EIT. In this paper, we investigate an incremental pathway towards 3D EIT reconstructions, using two electrode planes to calculate improved transverse slices as an intermediate step. We recommend a specific placement of electrode planes, and further demonstrate the feasibility of multi-slice reconstruction in two species.

Approach Simulations of the forward and reconstructed sensitivities were analysed for two electrode planes using a "square" pattern of electrode placement as a function of two variables: the stimulation and measurement "skip", and the electrode plane separation. Next, single- vs. two-plane measurements were compared in a horse and in human volunteers. We further show the feasibility of 3D reconstructions by reconstructing multiple transverse and, unusually, frontal slices during ventilation.

Main results Using two electrode planes leads to a reduced position error and improvement in off-plane contrast rejection. 2D reconstructions from two-plane measurements showed better separation of lungs, as compared to the single plane measurements which tend to push contrasts in the center of the image. 3D

reconstructions of the same data show anatomically plausible images, inside as well as outside the volume between the two electrode planes.

Significance Based on the results, we recommend EIT electrode planes separated by less than half of the minimum thoracic dimension with a "skip 4" pattern and "square" placement to produce images with good slice selectivity.

1. Introduction

Electrical Impedance Tomography (EIT) calculates images of the internal conductivity distribution within a body from applied electrical currents and voltage measurements at electrodes on the body surface. The most common medical applications of EIT have been on the thorax, in which the physiological parameters of interest are breathing- and heart-related movements of gasses, blood and fluids. A recent review (Frerichs *et al* 2017) described several thoracic applications in which EIT shows compelling benefits as a non-invasive monitoring modality. For lung ventilation and perfusion, EIT allows characterization of spatial distributions, which is important since many disease conditions result in dynamic and heterogeneous patterns. Most clinical and experimental EIT studies for thoracic imaging have used a single plane of electrodes, and have calculated a two-dimensional transverse image "slice". Such a single, representative slice is reasonable in many clinical applications, in which patients are in a supine (or prone) position, and where the most relevant inhomogeneities occur in the direction of gravity.

Unfortunately, a single electrode plane has many limitations, even for producing single transverse slice images. First, since electrical current propagates in a diffuse way, EIT is sensitive to a volume region above and below the electrodes, to a height of approximately $\frac{1}{2}$ of the body diameter (Adler *et al* 2015). This can interfere with EIT interpretation if changes occur outside the plane, such as in the abdomen (Ambrisko *et al* 2015) or to posture changes (Marquis *et al* 2006), which can move electrodes and deform the shapes of organs. In such cases, the location of out-of-plane effects will be false because no vertical information is available from the single-plane measurements. For many applications of EIT, it is natural to assume the spatial variation in conductivity is dominated by gravity-related effects. However, patients' lungs are very heterogeneous, as illustrated by contrasting-gas MRI images of obstructive lung disease (Kirby *et al* 2011) which show complex and diffuse patterns of aeration. Additionally, patients are often not perfectly supine, and, for many potential EIT applications, such as lung function or exercise testing, subjects are sitting or standing.

The solution is to reconstruct EIT in three dimensions. Of course, 3D reconstruction in EIT is not new. Early work (e.g. Rabbani and Kabir, 1991) studied the effect of off plane contrasts in two dimensional EIT. Metherall *et al* (1996) developed 3D EIT image reconstruction using a Moore-Penrose pseudo-inverse of the 3D sensitivity matrix. Subsequent authors have extended this approach to a regularized Gauss-Newton inverse

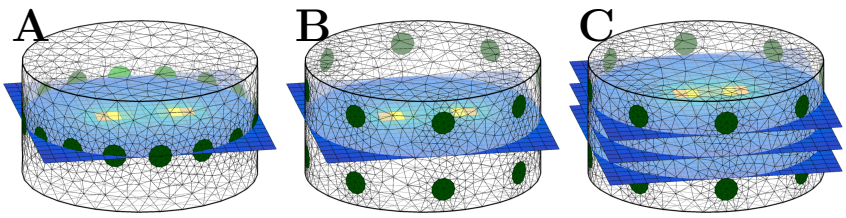

Figure 1. Illustration of the proposed pathway toward 3D EIT showing EIT reconstructions with: A) a single electrode and image plane, B) a single image plane with multiple electrode planes, C) multiple electrode and image planes.

(e.g. Blue *et al* 2000, Borsic *et al* 2010) or the GREIT algorithm (Ahn *et al* 2014). Other approaches have been used, such as the D-bar scattering transform (Knudsen *et al* 2009). We have also made recent contributions, formulating a 3D EIT version of GREIT (Grychtol *et al* 2016) and validating it using two-plane measurements as a function of posture (Wagenaar and Adler 2016, Grychtol and Adler 2018). Surprisingly, however, thoracic EIT – despite being the most common application of medical EIT – is the one where single-plane data acquisition is still the norm.

We are thus motivated to identify and address the issues which are holding back a move to 3D in the thoracic EIT community. We identify three issues: 1) the lack of an *incremental* pathway, which allows EIT users to benefit from 3D algorithms without changing their entire workflow and equipment; 2) a lack of detailed recommendations on where to place electrodes and what stimulation and measurement patterns to use; and 3) a concern about robustness – will 3D EIT be "finicky" and produce no useful results unless all measurement parameters are perfect?

This paper represents our contributions to these issues. Our main idea is to analyse methods that create improved single-slice images from multiple electrode planes. This represents an incremental pathway for users and EIT-system developers. Functional EIT image analysis and interpretation can be conducted as currently. For this usage, only two changes are needed: electrodes are placed differently and a new reconstruction matrix is calculated. The pathway is illustrated in figure 1 illustrates the options, showing (A) a single-slice image from single-plane electrodes, as well as two planes of electrodes from which either (B) single-slice or (C) volumetric images are calculated. We derive a formulation of the GREIT algorithm to calculate a single slice from a 3D arrangement of electrodes and contrast it with the conventional 2D arrangement. We also demonstrate the feasibility of volumetric reconstruction for lung EIT in humans and horses.

2. Methods: Overview

Our hypothesis is that a two-plane electrode placement for EIT can give improved single-plane cross-sectional images, versus a single plane placement of the same number of electrodes. Here "improved" is defined to mean a more accurate representation of internal conductivity changes, while maintaining or improving robustness to

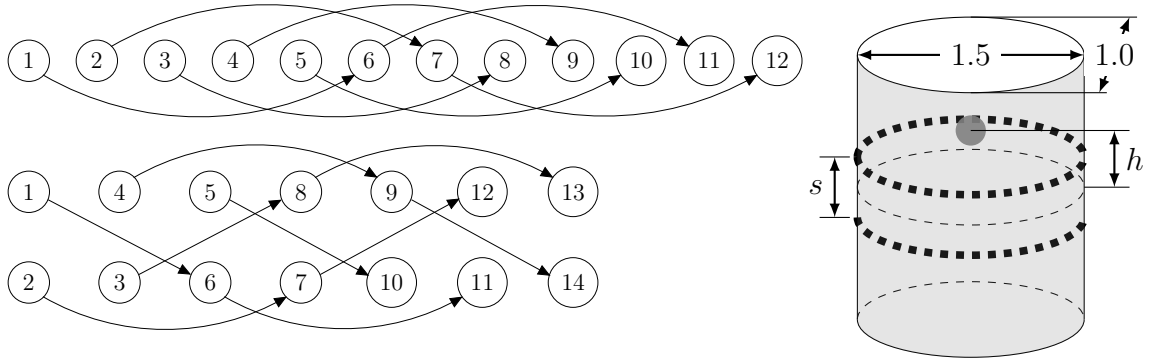

Figure 2. *Left:* Stimulation and measurement drive pairs (connected by arrows) using an EIT system with a *skip* = 4 pair drive and measurement configuration: (above) 1×32, and (below) 2×16 (using a "square" electrode layout) *Right:* Simulation and reconstruction geometry with electrode planes separated by s and a target h above the centre.

measurement configurations.

We address this hypothesis in two phases: first, a simulation study of 3D EIT measurement (section 3) and image reconstruction (section 4) sensitivity, with the goal of choosing a good 3D electrode configuration (in terms of plane separation and stimulation and measurement patterns); next, the selected configuration is studied in two species: horses (section 5.1) and humans (section 5.2).

There are clearly many possible multiple-plane EIT configurations. To narrow the scope, we use 32 electrode EIT systems with pair-drive and measurement, and consider two configurations: (1×32) a single transverse plane, and (2×16) two transverse planes, with electrodes arranged in a "square" pattern, illustrated in figure 2. We have previously argued that the square pattern is a good choice for two-plane EIT, in that half of the pair-drive patterns cross the planes vertically, while the other half are in-plane (Graham and Adler 2007, Grychtol *et al* 2016).

In this paper, we use the square patterns, and consider two main choices: the *skip* for the stimulation and measurement patterns, and the separation between electrode planes. Here, *skip* is the number of electrodes between the drive and receive electrode pairs, so an adjacent pattern has $skip = 0$ and stimulation between electrodes #1 and #6 has $skip = 4$. The planes are separated by a separation ratio, s, defined to be the ratio of the distance between planes to the minimum thoracic axis, and illustrated in figure 2. We define s in terms of the minimum axis, since EIT sensitivity will be larger for electrodes closest to the centre, corresponding to the anterior-posterior dimension in humans and the lateral width on the main animals on which EIT has been studied, such as horses, pigs and lambs.

3. Methods: EIT sensitivity

The sensitivity of an EIT system represents the expected change in measurements or images for small changes in internal conductivity. The spatial distribution of sensitivity is an important factor in an understanding of image reconstruction performance. A two- (vs one-) plane configuration creates a vertically broader sensitive region.

We use the following notation for time-difference EIT: a body starts with a baseline (i.e. before changes) conductivity distribution, $\boldsymbol{\sigma}^{(b)}$, represented by the elements of a body model. Linear time-difference EIT is sensitive to a change, $\Delta\boldsymbol{\sigma} = \boldsymbol{\sigma}^{(a)} - \boldsymbol{\sigma}^{(b)}$, between *after*, $\boldsymbol{\sigma}^{(a)}$, and *before*, $\boldsymbol{\sigma}^{(b)}$. A frame of voltage measurement data, $\mathbf{v}$, is acquired through a set of stimulation and measurement patterns. Measurement data are simulated using a forward problem, $F(\cdot)$, typically using a finite element model (FEM): $\mathbf{v}^{(b)} = F(\boldsymbol{\sigma}^{(b)})$ and $\mathbf{v}^{(a)} = F(\boldsymbol{\sigma}^{(b)} + \Delta\boldsymbol{\sigma})$. A measurement change vector, $\mathbf{y} = \mathbf{v}^{(a)} - \mathbf{v}^{(b)}$ is then calculated (or using the notation $\mathbf{y} = F(\mathbf{x})|_{\boldsymbol{\sigma}^{(b)}}$).

Images ($\mathbf{x}$) are parameterized from the forward model by a coarse-to-fine map, $\Delta\boldsymbol{\sigma} = \mathbf{M}\mathbf{x}$. Here, each element, $\mathbf{M}_{i,j}$, represents the volume fraction of forward-model region i contained within the image region j. The forward model requires a high density of mesh parameterization in areas near the electrodes (Grychtol and Adler, 2013), but the inverse image is parameterized onto a 3D voxel grid.

The sensitivity of measurement i to changes in voxel element j, is then given by the matrix, $\mathbf{J}_{i,j} = \frac{\partial \mathbf{y}_i}{\partial \mathbf{x}_j} = \frac{\partial}{\partial \mathbf{x}_j} F(\mathbf{x})|_{\boldsymbol{\sigma}^{(b)}}$. Assuming noise in each EIT measurement is equal and uncorrelated, the distinguishability of changes in voxel j from all measurements is the root-mean-squared sum $s_j = \|\mathbf{J}_{*j}\|_2$, where $*j$ represents the j^{th} column.

For simulations, we model the thorax shape (figure 4A) as an extruded elliptical FEM with major/minor axis ratio, 1.25. Lung regions were defined as ellipsoids and arm regions defined. The thorax was 2.6× longer vertically than the major axis and incorporates 300 k FEM elements. We choose a relatively simple simulation geometry to facilitate interpretation of the images. Onto the model, electrodes are placed as 1×32, or as 2×16, with a separation (s) of the minimum elliptical dimension. The choice of an elliptical thorax model was made to simplify interpretation, and to be roughly suitable for the two species evaluated.

Using this model, the vertical sensitivity of measurements is calculated by introducing small contrasts in each voxel in a frontal slice of the thorax and calculating the sensitivity s_j. Each sensitivity value is then normalized with the vertically-corresponding value in the electrode-plane (center plane between the electrode planes for the 2×16 setup), and shown (figure 3). In all cases, the 50% sensitivity contour covers approximately half the minimum thorax dimension in the centre. For 1×32, the region is more peaked from centre to edge, and this effect is increased for adjacent vs. $skip = 4$. These images display vertically-normalized sensitivity rather than raw sensitivity values, both to emphasize the off-plane contribution, and because EIT sensitivity is so strongly determined by the distance to the electrodes, that other effects are not visible.

We observe several features in the vertical sensitivity images. The “convex lens”

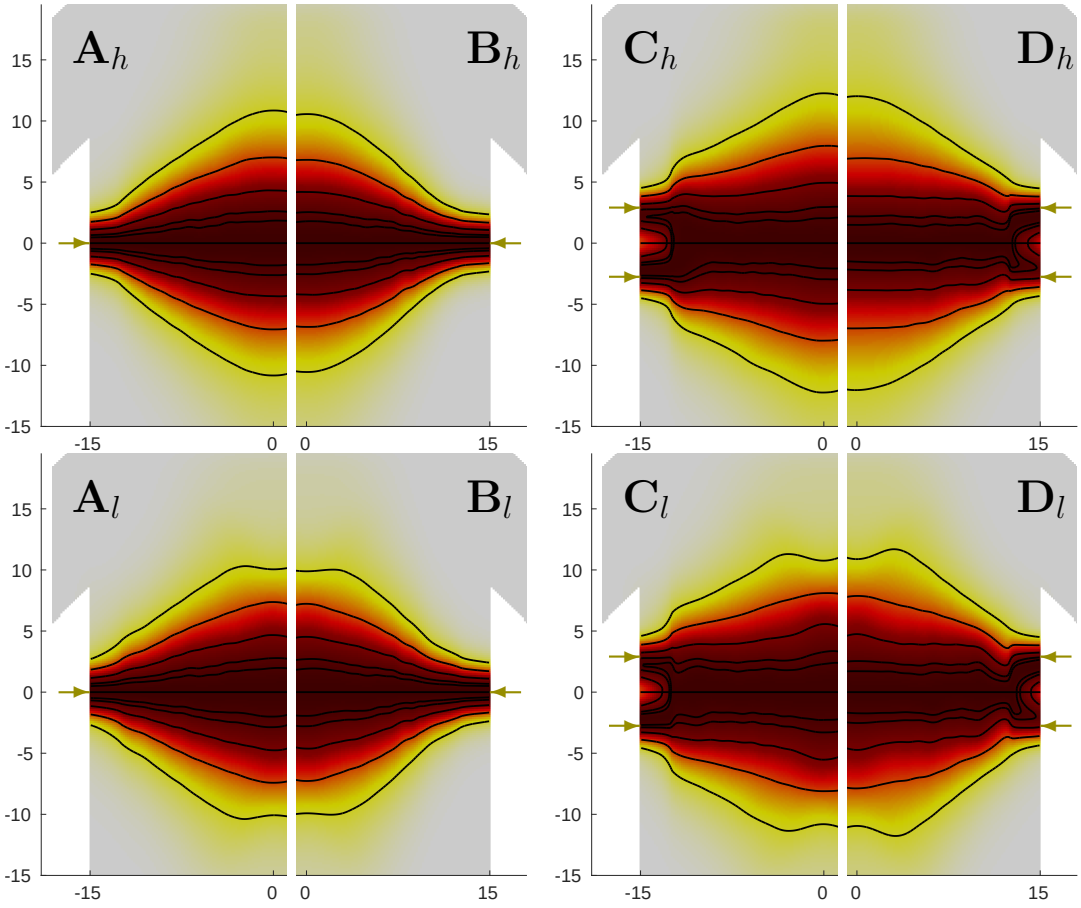

Figure 3. The vertical sensitivity of EIT in an elliptical thorax model (with added "arm" regions) sliced through the major axis (units in cm). The upper images (indicated $\cdot_h$ use a homogeneous conductivity model, while the lower images (indicated $\cdot_l$ use ellipsoidal lung regions). Pixel values are normalized with respect to the vertically corresponding mid-plane value, and relative sensitivity shown by the image and contours (indicating 95%, 90%, 75%, 50% and 25% of the maximum). Electrode planes are indicated by arrows, with A and B using 1×32, and C and D using 2×16. A and C use $skip = 4$, while B and D use $skip = 0$.

shape of the sensitivity is visible at both skip patterns and is only a little less pronounced with the 2×16 than the 1×32 arrangement. The use of two electrode planes creates a more homogeneous band of higher sensitivity in the central region between the planes, and also displays a lens shape at lower sensitivity. Finally, the presence of lower conductivity lungs (modelled at 0.3× background) disturbs mainly the sensitivity profile in the body centre (between the lungs).

4. Methods: Reconstructed image sensitivity

The reconstructed image sensitivity is not the same as the forward model sensitivity, since the goal of image reconstruction is to "separate" the relevant image parameters. Since EIT is theoretically capable of creating perfect images with sufficient

measurements (Sylvester and Uhlmann 1986), we here seek to understand how good EIT reconstruction can be with "only" 2×16 electrodes.

We use the formulation of GREIT developed in Grychtol *et al* (2016), which we briefly review to illustrate the relevant choices. Image reconstruction in difference EIT seeks to reconstruct a voxel image, $\hat{\mathbf{x}}$, parameterized from difference data, $\mathbf{y}$. Linear algorithms for difference EIT can be represented by a reconstruction matrix, $\mathbf{R}$, such that $\hat{\mathbf{x}} = \mathbf{R}\mathbf{y}$. The GREIT reconstruction matrix minimizes an error $\epsilon^2(\mathbf{R}) = \mathrm{E}_w\left[\|\mathbf{x} - \mathbf{R}\mathbf{y}\|^2\right]$ where w is the weight assigned to each target, $\mathbf{t}$, to represent the importance of its contribution. The expectation, $\mathrm{E}_w[\cdot]$ is over a distribution of "training" targets, $\mathbf{t}^{(i)}$, for which the corresponding data, $\mathbf{y}^{(i)}$, and a "desired" image, $\mathbf{x}^{(i)}$, are calculated. The reconstruction matrix which minimizes the error is $\mathbf{R} = \mathrm{E}_w\left[\mathbf{x}\mathbf{y}^T\right]\left(\mathrm{E}_w\left[\mathbf{y}\mathbf{y}^T\right]\right)^{-1}$.

Given a distribution $\mathbf{t} \sim \mathcal{N}(0, \mathbf{\Sigma}_t)$ of training targets, $\mathbf{x} = \mathbf{D}\mathbf{t}$ and $\mathbf{y} = \mathbf{J}\mathbf{t} + \mathbf{n}$ are calculated, where $\mathbf{J}$ is the Jacobian or sensitivity matrix, $\mathbf{D}$ is the "desired image" matrix, which maps each training sample location onto the larger desired image region as discussed above. Noise, $\mathbf{n}$, is distributed as $\mathbf{n} \sim \mathcal{N}(0, \mathbf{\Sigma}_n)$. Using these values

$$\mathbf{R} = \mathbf{D}\mathbf{\Sigma}_t^*\mathbf{J}^T\left(\mathbf{J}\mathbf{\Sigma}_t^*\mathbf{J}^T + \lambda\mathbf{\Sigma}_n\right)^{-1} \tag{1}$$

where $\mathbf{\Sigma}_t^*$ is the effective covariance of the training targets when weighted by w. The parameter λ is selected so that noise performance of the reconstruction matrix matches a prescribed noise figure value, with typical values between 0.5 and 2.

For robust 3D image reconstruction, it is important to introduce targets above and below the layers which form part of the reconstructed image. This requirement may be understood as "allowing" the image reconstruction to "explain" measurements via out-of-field contrasts. If not allowed to do this, the reconstruction will be "forced" to create artefacts in the image plane to account for these off-plane contrasts. We separate targets $\mathbf{t} = [\mathbf{t}_i|\mathbf{t}_o]$ into those inside, $\mathbf{t}_i$, and outside, $\mathbf{t}_o$, the reconstructed layers. The sensitivity matrix is similarly partitioned $\mathbf{J} = [\mathbf{J}_i|\mathbf{J}_o]$, and $\mathbf{D} = \mathrm{diag}(\mathbf{D}_i, \mathbf{D}_o)$. From (1), we calculate

$$\begin{bmatrix}\mathbf{R}_i\\ \mathbf{R}_o\end{bmatrix} = \begin{bmatrix}\mathbf{D}_i & 0\\ 0 & \mathbf{D}_o\end{bmatrix}\begin{bmatrix}A & B^T\\ B & C\end{bmatrix}\begin{bmatrix}\mathbf{J}_i^T\\ \mathbf{J}_o^T\end{bmatrix}\left(\begin{bmatrix}\mathbf{J}_i & \mathbf{J}_o\end{bmatrix}\begin{bmatrix}A & B^T\\ B & C\end{bmatrix}\begin{bmatrix}\mathbf{J}_i^T\\ \mathbf{J}_o^T\end{bmatrix} + \lambda\mathbf{\Sigma}_n\right)^{-1} \tag{2}$$

where A and C are the covariances of in- and outside plane targets, while B represents the covariance between them, and is typically small. Here the reconstruction matrix for the inside region,

$$\mathbf{R}_i = \mathbf{D}_i A\mathbf{J}_i^T\left(\mathbf{J}_i A\mathbf{J}_i^T + N\right)^{-1}, \tag{3}$$

where N represents data noise as well as the influence of out-of-plane contrasts, and $N = \lambda\mathbf{\Sigma}_n + \mathbf{J}_o B\mathbf{J}_i^T + \mathbf{J}_i B^T\mathbf{J}_o^T + \mathbf{J}_o C\mathbf{J}_o^T$.

The image reconstruction matrix depends on the details of the reconstruction model, represented through the target distribution and the hyperparameter λ (Grychtol *et al* 2016), and in the measurement configuration, represented in $\mathbf{J}$. Here, we identify and study three key aspects of the image reconstruction: 1) the separation between

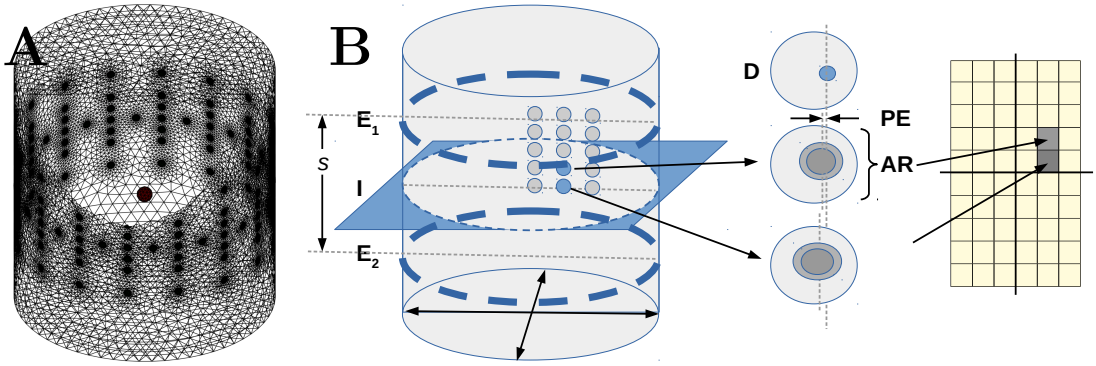

Figure 4. Evaluation methodology overview: A) FEM used for simulating sensitivity and reconstruction performance, B) Simulation strategy and figures of merit. For each target, an image is reconstructed on a plane, and the amplitude (AR) and position error (PE) with respect to the desired image (D) calculated.

the electrode planes, 2) the electrode stimulation and measurement pattern, and 3) the reconstruction noise amplification (corresponding to λ and the noise figure, NF).

The study of reconstructed image sensitivity is illustrated in figure 4. An elliptical model similar to that described in section 3 ($a = 1.5$, $b = 1.0$, $h = 3.0$, 1.1×10^6 elements) was constructed. To accommodate different electrode separations, a total of 192 electrodes were included in the FEM: a ring of 32 electrodes at the central plane $h_0 = 1.5$, and 5 pairs of 16 electrode rings located at $h = h_0 \pm s/2$ for separations $s \in \{0.2, 0.4, \ldots, 1.0\}$. Difference voltage measurements caused by a small contrast ($r = 0.05$, $\Delta\sigma = 1\%$) at various positions in the model were simulated.

The image reconstruction model was based on a (fine) FEM (0.8×10^6 elements) covering the same volume. The reconstruction (coarse) grid used a 44×65 (horizontal) $\times 65$ (vertical) voxel grid. Training targets used the sigmoid shape definition and were centred in each coarse grid voxel. Other parameters used the default values in EIDORS version 3.9 (Adler *et al* 2017). Parameter λ was selected by bisection search to ensure the reconstruction NF matched its chosen value.

Image reconstructions for each simulated contrast are evaluated in terms of the amplitude response (AR, or area-weighted sum of reconstructed image amplitude) in the central plane, the position error (PE) between the centre of gravity of the target ROI (pixels above 0.25 of the maximum value) and the desired image centre, and the target amplitude response (ART, or sum of image pixels in the target ROI). Values for individual positions are combined to create figure of merit maps as in (Grychtol *et al* 2016).

Simulation results are shown as a function of plane separation, s, (considering 1×32 to be $s = 0$) and noise figure. In each case, images are shown for $skip = 4$ and $skip = 0$ for homogeneous models. Figure 5 shows reconstructed images as a function of vertical off plane position h. We note that, especially for 1×32, there is a strong position error, with the reconstructed object too close to the centre, and also showing a ringing effect. For 2×16 configurations, almost no position error is apparent, and the

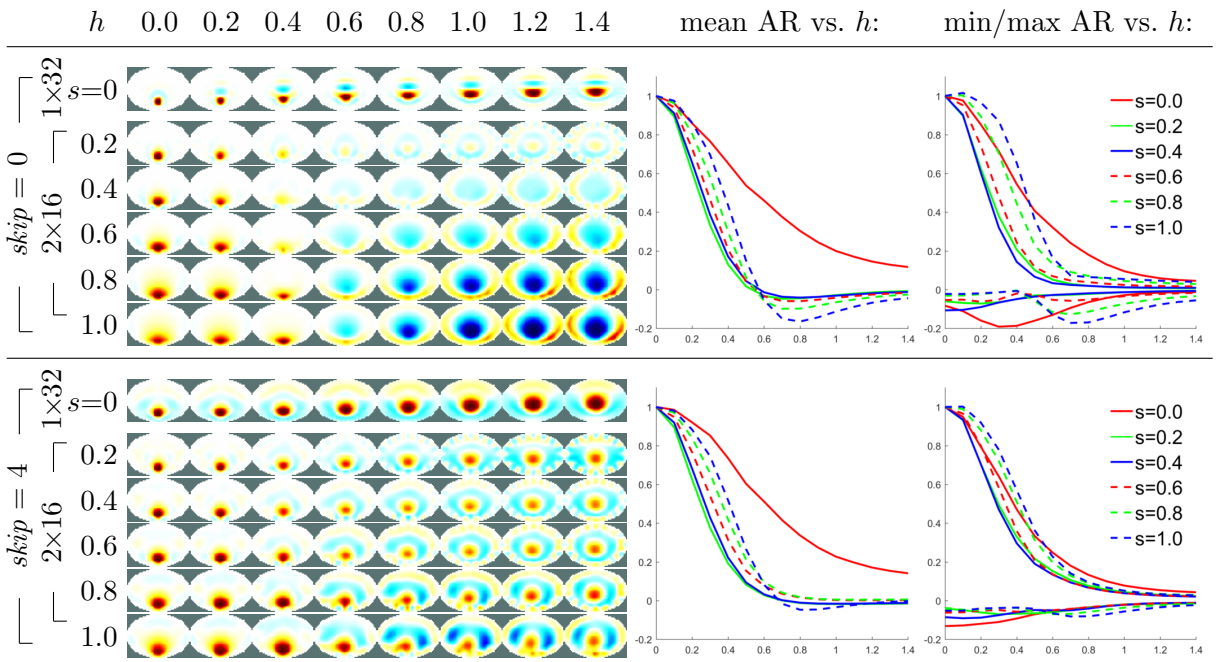

Figure 5. Reconstructed centre-slice images for an off-centre target moving vertically away from the centre plane, for NF=1 and the indicated plane separation. For each horizontal image h increases, while vertical image sequences have different plane separations s. Image amplitude is normalized to the 1×32 reconstruction at each h. Graphs show the mean, maximum and minimum image values as a function of h, normalized to $h = 0$.

contrast level decreases much more quickly with h. However, for the largest values of s, a low-amplitude negative image is shown. In terms of image artefacts, *skip*=4 performs better in terms of avoiding ringing and inverse artefacts.

The images in figure 5 show only the results at a specific horizontal target position. We calculate summary images of the image amplitude (figure 6) and position error (figure 7).

For all NF and skip values, the 2×16 arrangement offers better off-plane contrast rejection than 1×32. At the lower levels of regularization (i.e. higher NF), 1×32 has a highly peaked shape to its off-plane contribution. For 2×16, the regularity of shape of the central high sensitivity region varies with s. For values of s above 0.2, a consistent central band appears of approximately the size of the plane separation. As s increases beyond 0.6, the sensitive volume becomes quite large. Overall results for *skip=4* are less prone to artefacts and ringing than *skip=0*.

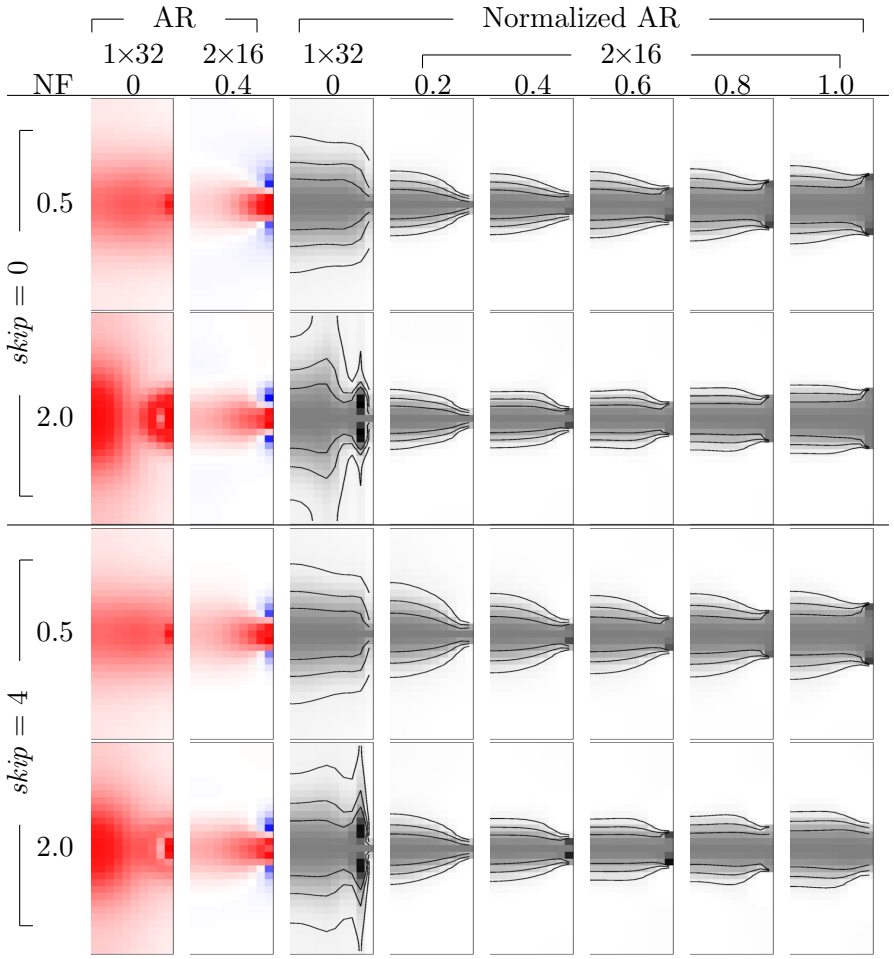

Figure 6. Amplitude response vs. Plane separation (s) as a function of s and regularization (NF). Each image represents a vertical slice quadrant of the amplitude response as illustrated in figure 4. The left two image columns show the raw AR value (red: positive, blue: negative), while the right image columns show AR normalized to its on-axis value in the centre plane, with contours at 75%, 50% and 25% and only positive values shown. Each image has horizontal axis from centre to minor-axis side and vertical axis from $h = -1.5$ to 1.5.

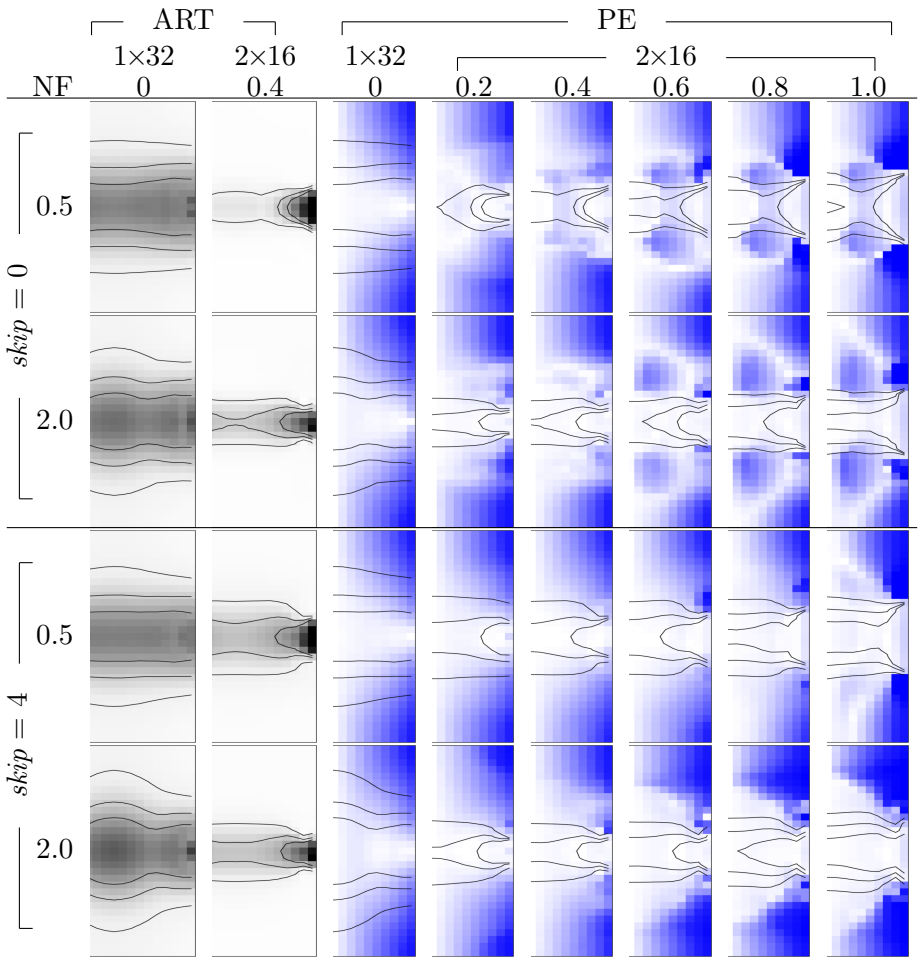

Figure 7. Position Error vs. Plane separation (s) as a function of s and regularization (NF). Each image represents a vertical slice quadrant of the position error as illustrated in figure 4. The left two image columns show the raw ART value (c.f. figure 6), while the right image columns show PE (red: away from centre, blue: toward the centre), with contours at 75%, 50% and 25% of the maximum ART for the same configuration. Each image has horizontal axis from centre to minor-axis side and vertical axis from $h = -1.5$ to 1.5.

5. Experimental Methods

In this section, we describe experimental validation of the developed algorithm in two models. Currently, belts designed for EIT electrodes are for single plane arrangements only, and thus two-plane EIT electrode placements need to be custom built. Figure 8 shows the arrangements used in the two experiments, including (A) a custom belt and (B) individual ECG-type electrodes.

5.1. Experimental Methods: Horses

In this section, we describe validation of the developed EIT algorithms in a horse model. The horses large lungs experience a large variation in the regional distribution of ventilation. The experiment was approved by the Institutional Ethics and Animal Welfare Committee of the Veterinary University Vienna under ETK-03/04/201. Data were acquired using $skip = 4$ stimulation and measurement pattern. from a single standing horse during quiet breathing (no sedation). A custom electrode belt was designed (figure 8), and applied to the horse with a normal hair coat (not clipped) and with electrode/ultrasound gel applied richly to maintain good contact.

The EIT electrode belt was developed to allow combined placement of both: (1×32) 32 electrodes in a single plane, and (2×16) two planes of 16 electrodes, each separated by 12 cm from the single plane and arranged in a "square" pattern. The arrangement allows measurements without removing and re-attaching the belt that may cause poor repeatability. Electrode were round with diameter 25 mm and mounted equidistantly. Using the BBVet system (SenTec, Landquart, Switzerland), data were acquired during quiet tidal breathing first using 1×32, and then switching the electrodes to 2×16 for

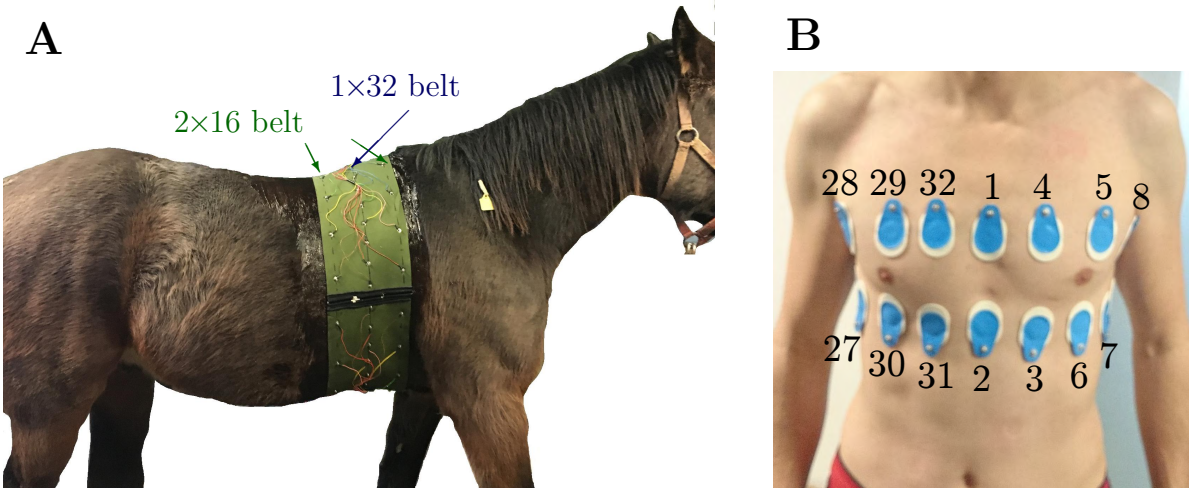

Figure 8. Electrode placement: A) an electrode belt placed on an awake upright horse. A 1×32 and 2×16 electrode configuration is included in the same belt. Ultrasound gel is used to improve electrode contact. B) 2×16 electrode configuration placed on a volunteer using individual electrodes (3D belts were not available).

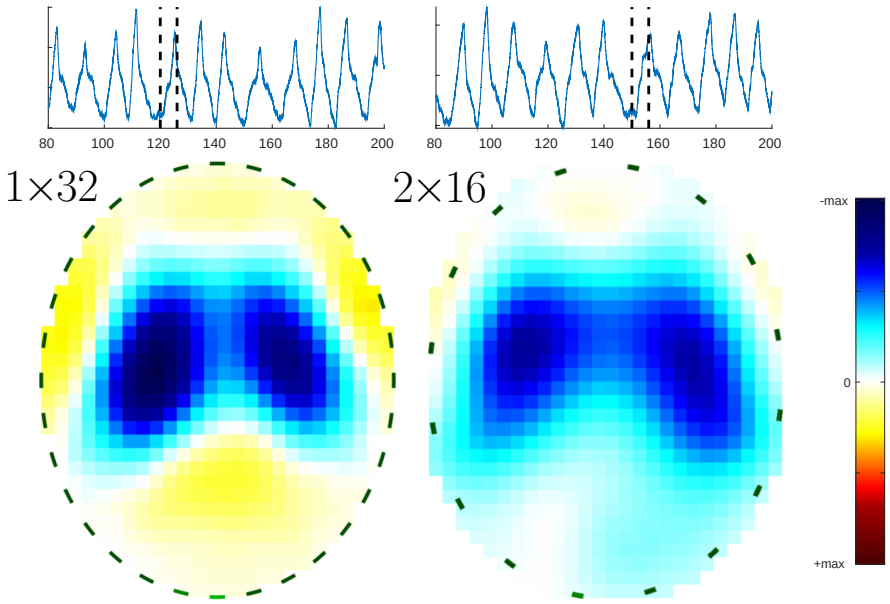

Figure 9. Reconstructed tidal ventilation images of the centre transverse plane for 1×32 (left) and 2×16 (right) electrode configurations.

subsequent acquisition. Images were reconstructed using GREIT with an elliptical model with major/minor axis ratio 1.25, and plane separation $s = 0.4$.

Reconstructed images are compared in figure 9, showing lung regions closer to the image centre in the 1×32 than the 2×16 image. This position error in the lung images is consistent with our simulation results. First, breath boundaries were identified in the raw data, and a representative tidal breath selected. Tidal ventilation fEIT images were then reconstructed of the conductivity change between end-expiration and end-inspiration.

In addition to images of the centre slice, it is possible to create 3D images in several ways, illustrated in figures 10 and 11. First, slices of volumetric images can be shown (left) in which it is possible to visualize the diagonal orientation of the horse's lungs above the diaphragm. The region of inverse contrast is likely to be the abdomen, which contains a large gas volume in the horse and will decrease in volume as the lungs expand (Ambrisko *et al* 2015). On the right side of the figure, the lung volume is shown as a function of time through the breath. At each time point, images can be shown of transverse (figure 10) or even frontal slices (figure 11).

The breathing time course shown in figure 10 shows large regional variations in the local time course of filling and emptying in each lung pixel. In order to further analyse these regional differences, representative pixels are chosen in transverse (ventral-dorsal) and frontal (cranial-caudal) directions, and the normalized pixel time courses plotted. (figure 12).

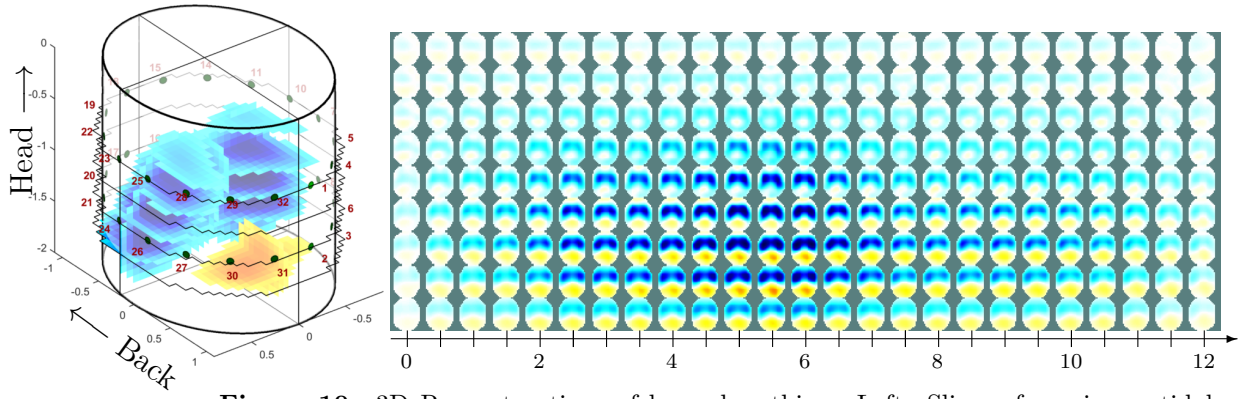

Figure 10. 3D Reconstructions of horse breathing. Left: Slices of maximum tidal ventilation image, Right: transverse plane images as a function of time (s) in a single breath.

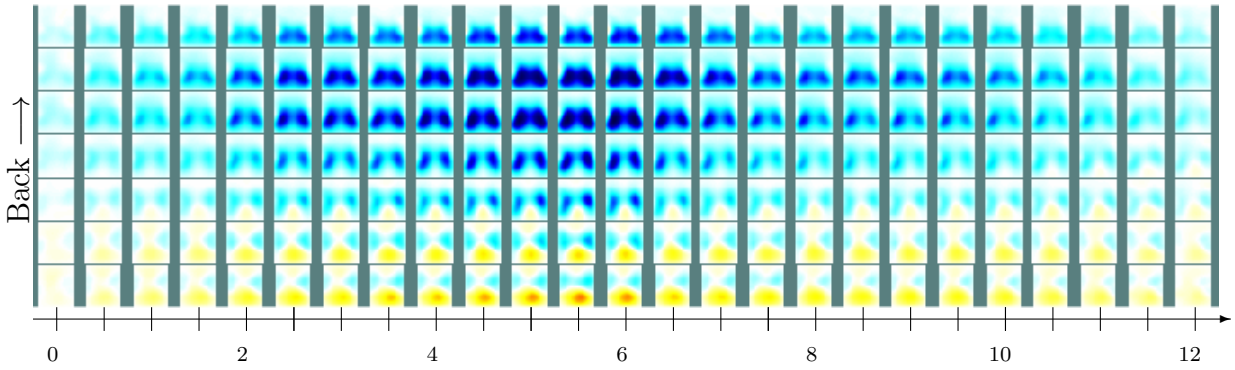

Figure 11. 3D Reconstructions of horse breathing - frontal slices (cf. figure 10.)

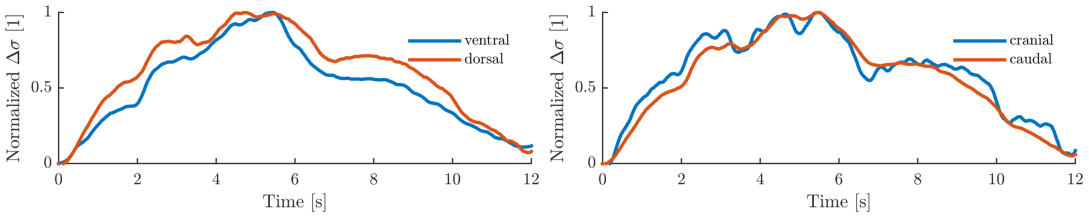

Figure 12. Respresentative pixel timecourses in: *left* ventral/dorsal direction, *right* cranial/caudal direction

5.2. Experimental Methods: Volunteers

Data from healthy volunteers were collected in a study of EIT-based stroke volume measurement (Braun *et al* 2018). Ten healthy adult volunteers (9 male/1 female, weight: 68.9 ± 10.8 kg, age: 35.4 ± 4.1 years) were enrolled in the study. Ethics approval was obtained from the ethics committee of the canton of Vaud, Switzerland (CER-VD, 2017-00709). Data during recovery after supine bicycle exercise was used (task 5 in Braun *et al* (2018)).

For each volunteer, 32 gel electrodes were placed on two planes with 16 electrodes each: one above and one below the nipple line (see figure 8B). Next, to create a subject-

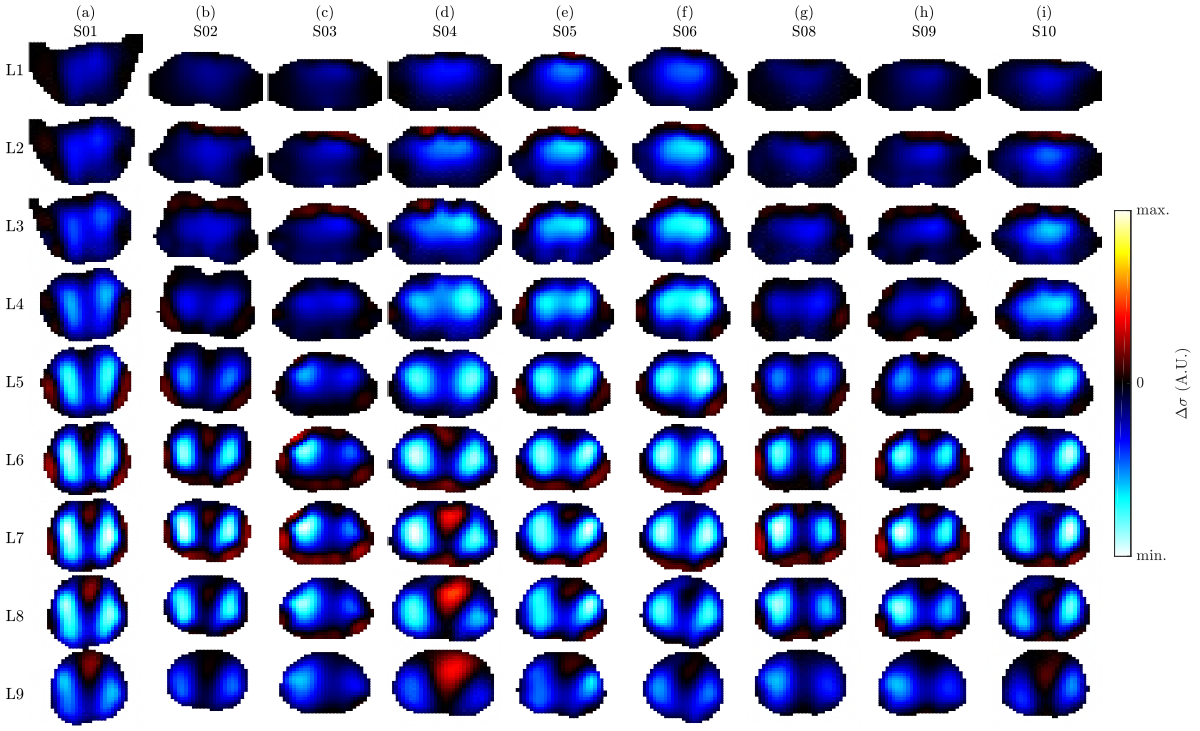

Figure 13. Tidal ventilation in healthy subjects in supine position. Nine image planes (vertical axis) for each subject (horizontal axis).

specific anatomical model with the correct electrode positions, a 3D surface of the subject's thorax was acquired using a dedicated software in combination with a 3D camera. EIT data were acquired with the BB^2 EIT device (SenTec AG, Landquart, Switzerland), via ECG cables connected to the traditional electrode belt. Electrodes were connected as shown in figure 8B which corresponds to a square pattern with $skip = 4$ stimulation and measurement configuration.

For each volunteer, a subject-specific FEM for EIT image reconstruction was created. Unused parts of the 3D thorax surface were cropped, the surface was smoothed, and a mesh with refined electrodes created using the approach of Grychtol and Adler (2013). EIT data were reconstructed with the 3D GREIT algorithm onto nine images planes, such that L3 corresponds to the upper and L7 the lower electrode planes.

Data for each subject in supine position was acquired and a breath identified by the end-expiration and -inspiration time points. Figure 13 shows a fEIT tidal volume image, reconstructed form these two data points, for nine image levels for each volunteer. Amongst these images we note that there are interesting variations in the 3D pattern of ventilation, showing a clear separation of lungs in lower planes and "connected" lungs in higher planes.

6. Discussion

In this paper, we are motivated by an apparent paradox: while thoracic phenomena are inherently three dimensional, and many 3D EIT algorithms exist, little use of 3D EIT imaging is being done. We then aim to address the three issues we perceive as holding back the move to EIT 3D imaging.

First, we propose an incremental pathway, using a 2×16 electrode configuration instead of the traditional 1×32, but where a single EIT-image slice is calculated. Our results appear promising, both in terms of the consistency of images produced and improved rejection of off-plane contrasts. Additionally, tools to calculate this single slice image have been contributed to EIDORS‡ (Adler *et al* 2006) as well as new reconstruction matrix software for the SenTec STEM software.

If multiple-plane measurements is used, there are many choices to make: how many planes and how far apart should the planes be? should electrodes planes be orthogonal to the imaging plane? what patterns of voltage measurement and current stimulation should be used? Here, we make the following recommendations: EIT electrodes should be placed in a 2×16 configuration with a plane separation, s, of less than half the minimum thoracic diameter. Electrodes should be placed in a "square" configuration, and stimulation and measurement pattern with an even "skip" value used.

Finally, to address the concern about whether 3D EIT would be sufficiently robust, we conducted pilot measurements in two species. A horse model is interesting because of their complex, three dimensional, pattern of breathing. Due to their size and specific anatomy, horse lungs are more exposed to gravity-related pressure changes during anaesthesia, and their large abdominal organs with huge amounts of gas lie, diagonally, directly ventral to the main parts of the lung. Thus, as the diaphragm moves and flattens during breathing, air is moved in and out of the plane of interest. Clinically, equine asthma is a very common disease with enormous diagnostic challenges, which introduces patchy inhomogeneous changes to lung function. EIT images with 2×16 configuration appear to correspond better to the anatomy than 1×32. First, lungs are less "pushed" toward the center (corresponding to reduced position error), and ringing artefacts appear to be reduced. We argue that the anatomically plausible and low-artefact reconstructions we present demonstrate good robustness of 3D difference EIT to the uncertainties typically present in lung EIT, such as imperfect knowledge of electrode locations or body shape.

Monitoring breathing in adult humans is currently the most important application of EIT. While smaller than horse lungs, human lungs also display important inhomogeneities due to the effects of gravity and disease processes. Obstructive lung diseases such as asthma and COPD produce diffuse regions of inhomogeneous ventilation with significant timing differences between lung regions (Kjellberg *et al* 2016), while many restrictive lung diseases are associated with increases in lung fluids which are pulled toward the dependent lung and create gravity-dependent patterns of

‡ eidors.org/tutorial/GREIT/GREIT3D_horse.shtml

inhomogeneous ventilation. The ability of 2×16 EIT to resolve the individual lungs in caudal slices while showing fused lung regions in cranial slices would be diagnostically useful. This is perhaps also an explanation of the variability across patients in EIT's ability to resolve the individual lungs.

In our simulation study of 3D imaging, we note that 2×16 outperforms 1×32 on almost all measures. Specifically, there is a significant position error for 1×32 as off-plane contrasts are reconstructed too close to the body centre, an effect which is virtually absent with 2×16. Off-plane contrasts also show increased ringing in the reconstructions. As with 1×32, a larger skip pattern (4) produces better images with larger sensitivity. This is especially the case with the highly peaked AR measure with an adjacent pattern. In our experience with these pilot measurements, 2×16 was at least as robust as 1×32. The use of the noise figure approach to setting hyperparameter values may not be completely satisfactory. Braun *et al* (2017) showed that for larger skip patterns the same NF leads to a more regularized image, which may explain some of the decrease in resolution. All algorithms, procedures and functionality presented in this paper is available in EIDORS version 3.9.1 (Adler 2018).

In summary, we recommend that experimental applications of thoracic EIT should be done in 3D whenever warranted by the physiological question. As an intermediate step, electrodes should be placed in a 2×16 pattern and a "drop-in" replacement for a 1×32 reconstruction matrix calculated. The key next steps are to design tools for 3D EIT analysis, to understand its stability, reproducibility and performance (e.g. does 2×16 reduce the sensitivity to electrode placement errors), and to design robust and comfortable electrode placement belts.

References

Adler A 2018 EIDORS version 3.9.1 *Zenodo* doi: 10.5281/zenodo.1257669

Adler A and Lionheart W R B 2006 Uses and abuses of EIDORS: An extensible software base for EIT *Physiol Meas* 27 S25–S42

Adler A Boyle A Braun F Crabb MG Grychtol B Lionheart WRB HFJ Tregidgo Yerworth R EIDORS Version 3.9 p 63, *Proc EIT2017*, Dartmouth, NH, USA, Jun 2–5

Adler A Frerichs I Grychtol B 2015 "The off-plane sensitivity of EIT", p 68, *Proc EIT2015*, Neuchâtel, Switzerland, Jun 2–5

Ahn S Wi H Oh TI McEwan AL Jun SC Woo EJ 2014 Continuous Nondestructive Monitoring Method Using the Reconstructed Three-Dimensional Conductivity Images via GREIT for Tissue Engineering *J Applied Math* 562176

Ambrisko T Schramel J Adler A Kutasi O Makra Z Moens Y 2015 Assessment of distribution of ventilation by electrical impedance tomography in standing horses *Physiol Meas*, 37 175–186.

Bayford RH Kantartzis P Tizzard A Yerworth R Liatsis P and Demosthenous A 2008 Development of a neonate lung reconstruction algorithm using a wavelet AMG and estimated boundary form *Physiol Meas* 29 S125–S138

Blue RS Isaacson D and Newell JC 2000 Real-time three-dimensional electrical impedance imaging *Physiol Meas* 21 15–26

Borsic A Halter R Wan Y Hartov A and Paulsen KD 2010 Electrical impedance tomography reconstruction for three-dimensional imaging of the prostate. *Phys Meas* 31 S1–S16.

Braun F Proença M Adler A Riedel T Thiran J-P Solà J 2018 Accuracy and Reliability of Noninvasive

Stroke Volume Monitoring via ECG-Gated 3D Electrical Impedance Tomography in Healthy Volunteers *PLoS One*, 13:e0191870.

Braun F, Proença M, Solà J, Thiran J-P, Adler A 2017 A Versatile Noise Performance Metric for Electrical Impedance Tomography Algorithms *IEEE T Biomed Eng* 64:2321–2330

I Frerichs, M Amato, A Van Kaam, D Tingay, Z Zhao, B Grychtol, M Bodenstein, H Gagnon, S Böhm, E Teschner, O Stenqvist, T Mauri, V Torsani, C Luigi, A Schibler, G Wolf, D Gommers, S Leonhardt, A Adler *Thorax*, 72:83–93, 2017.

Graham B and Adler A 2007 Electrode Placement Configurations for 3D EIT *Physiol Meas*, 28 S29–S44

Grychtol B and Adler A 2018 Separation of 3D EIT electrode planes p.62, *Proc EIT 2018*, Edinburgh, UK, June 11–13

B Grychtol, B Müller, A Adler "3D EIT image reconstruction with GREIT", *Physiol Meas* 37:785–800, 2016.

Grychtol B and Adler A 2013 FEM electrode refinement for Electrical Impedance Tomography *Conf IEEE Eng Med Biol Soc*, pp. 6429–6432, Osaka, Japan, July 3–7

Kirby M Mathew L Heydarian M Etemad-Rezai R McCormack DG Parraga G 2011 Chronic Obstructive Pulmonary Disease: Quantification of Bronchodilator Effects by Using Hyperpolarized He MR Imaging *Radiology* 261:283–292

S Kjellberg, BK Houltz, O Zetterström, PD Robinson, Per M Gustafsson, 2016 "Clinical characteristics of adult asthma associated with small airway dysfunction" Respir Medicine 117:92–102

Knudsen K Lassas M Mueller JL and Siltanen S 2009 Regularized D-bar method for the inverse conductivity problem. *Inverse Problems and Imaging* 35:599–624

Marquis F, Coulombe N, Costa R, Gagnon H, Guardo R, Skrobik Y 2006 Electrical Impedance Tomography's Correlation to Lung Volume is Not Influenced by Anthropometric Parameters *J Clinical Monitoring and Computing* 20:201–207

Metherall P, Barber DC, Smallwood RH, Brown BH "Three dimensional electrical impedance tomography", *Nature* 380:509-512, 1996.

Rabbani KS and Kabir ABMH 1991 Studies on the effect of the third dimension on a two dimensional EIT system *Clin Phys Physiol Meas* 12: 393–402

J Sylvester, G Uhlmann, 1986 "A uniqueness theorem for an inverse boundary value problem n electrical prospection" *Comm Pure Appl Math* 39:91–112.

J Wagenaar, A Adler, "Electrical impedance tomography in 3D using two electrode planes: characterization and evaluation", *Physiol Meas*, 37:922–937, 2016.